



## Article

# An Invitation on Characterization of H<sub>2</sub>-Reduced Bauxite Residue and Recovering Iron through Wet Magnetic Separation Processes

Ahmad Hassanzadeh <sup>1,\*</sup> , Ganesh Pilla <sup>2</sup> , Manish K. Kar <sup>3</sup>  and Przemyslaw B. Kowalczyk <sup>1</sup> 

<sup>1</sup> Department of Geoscience and Petroleum, Faculty of Engineering, Norwegian University of Science and Technology, 7031 Trondheim, Norway; przemyslaw.kowalczyk@ntnu.no

<sup>2</sup> Department of Materials Engineering, KU Leuven, Kasteelpark Arenberg 44, 3001 Leuven, Belgium; ganesh.pilla@kuleuven.be

<sup>3</sup> Department of Materials Science and Engineering, Norwegian University of Science and Technology, Alfred Getz vei 2, 7491 Trondheim, Norway; manish.k.kar@ntnu.no

\* Correspondence: ahmad.hassanzadeh@ntnu.no; Tel.: +49-17620666711

**Abstract:** Recovering iron from the bauxite residue (BR) is one of the long-standing challenges in the mining industry. However, there is a substantial lack of information in the literature regarding sample properties and iron extraction by reducing hydrogen. The present study aims at reducing a Greek BR using hydrogen, its characterization, and separating iron by magnetic separation processes. To this end, the reduced sample was characterized using X-ray diffractometry analysis (XRD), X-ray fluorescence spectrometer analysis (XRF), thermomagnetic analysis (TMA), automated mineralogy (AM), and scanning electron microscopy (SEM) coupled with energy dispersive spectroscopy (EDS). The effect of particle size ( $-200 + 100 \mu\text{m}$ ,  $-100 + 75 \mu\text{m}$ , and  $<75 \mu\text{m}$ ) was investigated through a medium-intensity magnetic separation (MIMS, Davis Tube) at 1000–2500 Gauss and a Slon<sup>®</sup> magnetic separator (1000 G). The effects of solid content (3% and 10% *w/w*) in a wet low-intensity magnetic separation (WLIMS, 350 G) and a two-stage MIMS followed by WLIMS were investigated. It was revealed that through reduction at 500 °C and 2 h with 20 wt% NaOH under 5 vol.% H<sub>2</sub> + 95 vol.% N<sub>2</sub>, iron oxides and ferric oxyhydroxide (Fe<sub>2</sub>O<sub>3</sub> and FeOOH) were converted into magnetite (Fe<sub>3</sub>O<sub>4</sub>), whereas aluminum (oxy)hydroxides (Al(OOH), Al(OH)<sub>3</sub>) were reacted with Na<sup>+</sup> towards sodium aluminates (NaAlO<sub>2</sub>). The AM observations indicated that only 3% of iron was in the phase of liberated magnetite, and the remaining was associated with Na, Al, and Ti phases with different intensities. The dissemination of iron throughout the matrix of the sample was recognized as the principal challenge in the physical separation processes. It was found that increasing magnetic intensity from 1000 G to 2500 G resulted in improved recovery for all studied particle size fractions in Davis Tube tests. The particle range of  $-106 + 74 \mu\text{m}$  was chosen as the most appropriate size to achieve the maximum Fe content of 41%. The results of WLIMS (350 G) showed the maximum Fe grade but revealed less recovery of 52% and 27% at 10% and 3% solid contents, respectively, compared to the Davis Tube trials.

**Keywords:** H<sub>2</sub>-reduced bauxite residue; wet magnetic separation; magnetic field and particle size; magnetite; grade and recovery



**Citation:** Hassanzadeh, A.; Pilla, G.; Kar, M.K.; Kowalczyk, P.B. An Invitation on Characterization of H<sub>2</sub>-Reduced Bauxite Residue and Recovering Iron through Wet Magnetic Separation Processes. *Minerals* **2023**, *13*, 728. <https://doi.org/10.3390/min13060728>

Academic Editor: Longhua Xu

Received: 24 April 2023

Revised: 16 May 2023

Accepted: 22 May 2023

Published: 26 May 2023



**Copyright:** © 2023 by the authors. Licensee MDPI, Basel, Switzerland. This article is an open access article distributed under the terms and conditions of the Creative Commons Attribution (CC BY) license (<https://creativecommons.org/licenses/by/4.0/>).

## 1. Introduction

The hydrometallurgical Bayer process is the main method for producing alumina through the dissolution of high-quality bauxite resources with a silicon modulus (Al<sub>2</sub>O<sub>3</sub>/SiO<sub>2</sub>) greater than seven into hot NaOH (sodium hydroxide) at elevated pressures [1]. As this approach is very energy-intensive, alumina plants/refineries are mainly located near relatively inexpensive coal power stations, which ultimately leads to substantial CO<sub>2</sub> emissions and serious environmental issues such as contamination of underground water and air pollution [2]. In

addition to that, alumina production is associated with the generation of waste, so-called red mud (RM) or bauxite residue (BR), which is highly alkaline ( $\text{pH} > 10.5\text{--}13$ ) and very fine in particles. Statistically and technically speaking, per each ton of alumina production, about  $1\text{--}1.5\text{ m}^3$  of bauxite digestion residue is generated worldwide [3,4]. This indicates piling ca. 120 to 150 million  $\text{m}^3$  of BR in tailing dams annually [5]. Depending on the ore type and process efficiencies, such tailings contain ca. 35–55% iron and invaluable critical elements (e.g., Ti, Cr, and rare earth elements (REEs)). Over the years, many applications have been addressed for re-using BRs, e.g., as heavy metal absorbents, for iron and critical metal extractions, as building materials and construction bricks, in cement production and road construction, as desulfurizer, and as pigment [6–8]. Nevertheless, these valorization processes are very limited when it comes to an industrial scale, mainly due to the alkalinity of the material, high transportation costs, and scale-up obstacles. The result is, as Evans [4] reported, that less than 3% of the annually generated BR is currently used globally.

To diminish  $\text{CO}_2$  emissions, hydrogen ( $\text{H}_2$ ) has been introduced as a reductant mainly in the steel and metal production industries [9,10]. By extracting iron from BRs, not only a significant amount of alumina tailings can be valorized, but specifically, Fe can be potentially recovered and employed for steel-making purposes. Several researchers reported feasible recovery of iron from BRs, but less practical information is available in the case of using  $\text{H}_2$  as a reductant. In this regard, Li et al. [11] applied a high-gradient superconducting magnetic separation (HGSM, 2–4 T) to separate iron from a BR with a fine particle size of  $<100\text{ }\mu\text{m}$ . Two types of this residue were subjected to processibility experiments RM1 and RM2, containing  $\text{Fe}_2\text{O}_3$  amounts of about 60% and 30%, respectively. According to their results, 65% and 45% of Fe were recovered for RM1 and RM2, with only 10% mass recovery in one stage. The intergrowth of Fe and its association with other elements were identified as the main challenges in that work. In another investigation, Rai et al. [12] studied the iron extraction from a BR ( $d_{80}$  of ca.  $50\text{ }\mu\text{m}$ , the specific gravity of  $3.3\text{ g/cc}$ , and  $\text{Fe}_2\text{O}_3$  content of 52%) through various advanced physical techniques such as single-stage and multistage magnetic separation, reduction roasting (calcination of RM with carbon present in wastes to be used as reducing agent), and hydrocyclone. The maximum  $\text{Fe}_2\text{O}_3$  content that could be reached was 60% under single/multiple stages of magnetic separation with intensities up to 15,000 G, using different reductants. It was concluded that the  $\text{Fe}_2\text{O}_3$  content was increased from 52% to 70%, with a recovery of about 80%, by adopting the hydrocyclone and magnetic separation routes. Cardenia et al. [13] endeavor to develop and optimize a reductive roasting process followed by a wet magnetic separation for iron recovery from a BR taken from Mytilineos S.A. ( $\text{Fe}_2\text{O}_3 = 42\%$ ,  $d_{50}$  of ca.  $2\text{ }\mu\text{m}$ ). It was reported that applying two stages of the wet high-intensity magnetic separator at 0.05 A followed by treating its concentrate with 0.1 A led to reaching 38% Fe concentrate. However, no information was found about the mass recovery for those experiments, and all of the above processes are carbon-based reduction methods. It was also addressed that the ceramic-forming constituents (especially  $\text{Al}_2\text{O}_3$ ) needed to be eliminated from the residue before its reductive roasting so that the separation of magnetic iron phases from the non-magnetic matrix could be performed effectively. Kapelari et al. [10] mixed a Greek BR ( $\text{Fe}_2\text{O}_3 = 42\%$ ) with NaOH and roasted it at  $600\text{ }^\circ\text{C}$  with pure  $\text{H}_2$  gas to produce water-soluble Na-aluminates and the  $\text{Fe}^{3+}$  content, respectively. The thermal treatment, followed by the water leaching process led to  $\text{Fe}_2\text{O}_3$  contents of 35% and 52%, respectively. Following these processes by grinding the sample ( $d_{50} = 5\text{ }\mu\text{m}$ ) and dry magnetic separation, the  $\text{Fe}_2\text{O}_3$  content increased from 35 wt% to 38 wt% (54%  $\text{Fe}_2\text{O}_3$ ), whereas using wet magnetic separation resulted in 32 wt% Fe. As seen from these case studies, the ultimate Fe percentage and its recovery were highly dependent on the applied process. It is worth noting that, for a profound perception of each process, one should pay attention to the ore properties, particle size, iron oxide contents in the feed, and reduction procedures for each case individually.

There is a considerable lack of information regarding downstream process treatments of  $\text{H}_2$ -reduced BR in the literature. This work, for the first time, endeavors to fill this

knowledge gap by studying the hydrogen reduction of a Greek BR followed by three different wet magnetic separators, with a special focus on the impact of particle size and magnetic field.

## 2. Materials and Methods

### 2.1. Sample Preparation

The initial BR taken from a Greek tailing disposal was reduced by hydrogen under optimum conditions (i.e., 5 vol.% H<sub>2</sub> gas at a respective temperature and time of 500 °C and 2 h with 20 wt% NaOH). As the focus of this study is mainly related to iron separability and its feasibility studies, detailed information regarding the reduction process and its methodology is not presented in this work and can be found elsewhere [9,14]. The reduced samples were received in the form of 1–2 cm pellets. The size of the pellets was reduced using a jaw crusher (Retsch, BB100, Haan, Germany), classified by a dry sieving method (RX-29H&B, ROT-AP<sup>®</sup>, W.S. Tyler, Mentor, OH, USA), and also measured by the laser particle size analyzer (LPSA, Mastersizer 3000, London, UK). As a normal procedure, the jaw crusher was cleaned up a few times with quartz and then ethanol to prevent any external contamination. The samples, after being ground and reaching desirable size fractions, were subjected to different equipment for separation purposes.

### 2.2. Characterisation Methods

For the characterization of the feed, X-ray diffraction (XRD), X-ray fluorescence spectrometry (XRF), inductively coupled plasma mass spectrometry (ICP-MS), SEM (scanning electron microscopy), coupled with EDS (energy-dispersive X-ray spectroscopy), automated mineralogy (AM), and thermomagnetic analysis (TMA) [15–18] were employed.

#### 2.2.1. XRD Measurements

The mineralogy of the raw BR, H<sub>2</sub> reduced BR, and magnetic and non-magnetic products was evaluated by X-ray diffraction (XRD) on a D2 phase diffractometer (Bruker D2 Phaser) and quantified (QXRD) by Rietveld analysis with TOPAS Academic [19–21]. The samples were measured between 10–65° 2θ using CuK radiation with an accelerating voltage of 30 kV and a current of 10 mA, with a step size of 0.02° and a counting duration of 0.8 s/step. The mineral phases in powder samples were quantified (QXRD) by adopting an external standard method with crystalline rutile (G-factor approach) [22]. The software DiffracEVA V4.1 (structures using the ICDD PDF2 database) and TOPAS-Academic V5 (structures from the ICDD database) were used for qualitative and quantitative analyses, respectively.

#### 2.2.2. XRF Analysis

The chemical composition of H<sub>2</sub>-reduced BR was measured using Wavelength Dispersive X-ray Fluorescence (WDXRF) spectroscopy. The analyses were performed on a 4 kW Bruker S8 TIGER (sequential WDXRF spectrometer with rhodium anode). A mixture of 1.4 g of the BR, 12.6 g of lithium borate, and 20 drops of lithium bromide was fused at 1050 °C to prepare glass beads via borate fusion for WDXRF chemical analysis.

#### 2.2.3. ICP-MS Analysis

To rely on the results obtained through the XRF and pXRF, the feed sample was also analyzed using ICP-HR-MS Element 2 (Thermo), equipped with an auto-sampler SC2 DX dust-covered with a ULPA filter. For this measurement, 0.5 g of the powder was used and dissolved in nitric acid (HNO<sub>3</sub>). The error was no more than 10%, as estimated by duplicating random points and inductively coupled plasma mass spectrometry (ICP-MS).

#### 2.2.4. SEM-EDS Measurement

The microstructure of solid H<sub>2</sub>-reduced BR products was analyzed by scanning electron microscopy (SEM Philips XL30 FEG model) coupled with energy dispersive spectroscopy (EDS) attached to it to examine the changes in mineral phases and microstructure

of reduced products. For SEM-EDS examination, samples were dispersed and mounted in epoxy resin, ground with silicon carbide sheets, and polished with an oil-based diamond suspension (3  $\mu\text{m}$  and 1  $\mu\text{m}$  diamond particles). The specimens were coated with 15 nm of carbon after being polished to ensure the optimal conductivity of the sample.

#### 2.2.5. TMA Analysis

The ground feed ( $\text{H}_2$  reduced BR) sample was subjected to a rotary splitter (Retsch, Germany) to obtain a representative sample for TMA measurements. Temperature-dependent magnetic susceptibility tests were performed using AGICO Inc., (MFK1-FA Kappabridge, Brno, Czech Republic) equipped with a CS-4 furnace and a CS-L cryostat using an AF-field amplitude of 200 A/m (0.25 mT). A 0.1–0.2 g of the specimen, together with a test tube and thermometer, were weighed. The equipment was run at high temperatures, while the magnetic susceptibility was determined incrementally as the sample was heated from room temperature (25 °C) to 700 °C and cooled down to 25 °C. Argon gas was injected into the tube with a flow rate of 6–8 L/h to inhibit the sample oxidation. The obtained results were analyzed through Cureval version 8.0.2 software. A detailed description of the measurement can be found elsewhere [15].

#### 2.2.6. AM Analysis

Automated mineralogy is a technique that combines SEM and energy dispersive spectrometry (EDS) to provide detailed mineralogical information on grain/particle sizes, modal mineralogies, mineral associations, and liberation degrees. More specific details regarding this technique and standard procedures can be found elsewhere [18,23]. To prepare the samples for SEM-based automated mineralogy measurements, a representative 2 g of the feed sample was put into a small glass container. Later, ca. 0.5 g graphite was added to the container, and the entire sample was homogenized by manual shaking for 5–10 min. It was later mounted in epoxy resin and subsequently polished to create a regular 25 mm polished section, which was cut into four and put into the 30 mm mound. Afterward, using epoxy resin again, 30 mm polished sections were created and coated before the scanning electron microscopy. For the SEM analyses, 10 nm of carbon coating was applied to the sample surface. Prior to the automated analyses, the sample was manually investigated using the ZEISS Sigma 300VP field emission SEM at GEUS, which was equipped with two Bruker Xflash, 129 eV energy dispersive spectrometry detectors, and a Bruker e-Flash FS EBSD detector. The SEM included the automated mineralogy software platform Mineralogic from ZEISS for AQM-SEM analyses. The Zeiss SUPRA 55VP was used for the back-scatter images (BSEs), and the microscope settings were 20 kV acceleration voltage, aperture 120, working distance 8.5 mm under mapping mode of 8% field overlap, 357.3 $\times$  magnification, 2.5  $\mu\text{m}$  step size (also pixel size), and 2000 counts in the spectrum, and 319 nm per pixel size. In AQM-SEM, energy-dispersive X-ray spectra were collected systematically covering a high-resolution grid in the analyzed Fe-bearing phases, and subsequently, each individual EDS spectrum was identified as a phase.

### 2.3. Magnetic Separation Tests

Three pieces of equipment were used for magnetic separation experiments, including a Davis Tube, Slon<sup>®</sup>, and a low-intensity magnetic separator (LIMS). The purpose of using Davis Tube was to identify the optimum particle size and magnetic intensity suitable for the studied material on a bench scale. The Slon<sup>®</sup> was used to evaluate the effect of particle size at a constant magnetic gradient of 1000 G, taking advantage of both magnetic and gravitational forces simultaneously. The LIMS was operated to analyze the effect of solid content at low (3% *w/w*) and high (10% *w/w*) magnitudes at a low permanent magnetic field of 350 G.

### 2.3.1. Davis Tube Tests

A Davis Tube (0.02–0.6 T, Dings Magnetic Separator Co., U.S.A.) was operated in two magnetic fields of 1000, and 2500 G, respectively, for three different feed size fractions, i.e.,  $-212 + 106 \mu\text{m}$ ,  $-106 + 74 \mu\text{m}$ , and  $<105 \mu\text{m}$ . For each test, 20 g of a representative sample was used, keeping the operation time almost constant. First, the strike was regulated at 60 stroke/min and the water flow rate was stabilized at 1 L/min. The prepared sample was added, and the non-magnetic product was gathered from the bottom of the tube, while the magnetic product was obtained by disconnecting the magnetic field at the end of the experiment. Both products were filtered, dried overnight at 60 °C in a laboratory oven, weighed, and then analyzed using the pXRF method (pXRF, Thermo Fisher Scientific). Three different points were randomly measured, and for each point, three measurements were adjusted using the equipment. Finally, the average values were reported as the final elemental contents. The iron recovery was calculated using Equation (1):

$$R(\%) = \frac{C}{F} \times \frac{c}{f} \times 100 \quad (1)$$

where  $R(\%)$  is the recovery,  $C(\text{g})$  and  $F(\text{g})$  are the weight of magnetic and non-magnetic products, and  $c(\%)$  and  $f(\%)$  denote the grade of Fe in the magnetic product and the feed sample, respectively.

Each experiment was repeated once, and the experimental errors were reported based on a 95% confidence level of those two tests.

### 2.3.2. Slon<sup>®</sup> Tests

As the sample contained disseminated magnetite, the lowest level of magnetic intensity (1000 G) was applied using the Slon<sup>®</sup> separator. First, one cleaning stage was executed by flushing water through the hoses and the equipment. Afterward, a suitable matrix according to the particle range was chosen. Later, the feed water flow rate given to the equipment was kept constant (5 L/min, 40.9 Hz) using an adjustable pump. The water underflow was regulated in such a way that the level of water in the cylinder was at the set point. The experiment was executed by applying a 1000 G magnetic field as the minimum possible field, and the sample was added to the cylinder afterward. The non-magnetic sample was first gathered, ensuring only water passed through the Slon<sup>®</sup>. After gathering the product, the magnetic field was reduced to zero, and the magnetic product was collected. Both samples were filtered, dried, weighed, and subjected to pXRF analyses. The experiments were repeated once, and the experimental errors were calculated with a 95% confidence level based on two experiments carried out under identical conditions.

### 2.3.3. LIMS Trials

In addition, two wet low-intensity magnetic separation tests, with a fixed low-magnetic intensity of 350 G, were examined under 3% ( $w/w$ ) and 10% ( $w/w$ ) solid concentrations on a feed size of  $-212 + 106 \mu\text{m}$ . The prepared samples were well mixed using a pump before feeding to the separator. The level of water within the cell was stabilized by regulating the feed and wash water used for cleaning the drum surface. After a steady state condition was reached, the slurry fed to the cell was separated into non-magnetic and magnetic products. Similar to the Davis Tube tests, all samples were filtered, dried, weighed, and characterized. Water properties were analyzed using ICP-MS in the chemistry laboratories of the Norwegian University of Science and Technology (Table A1, Appendix A). As an additional experiment, one medium-intensity (3000 G) magnetic separation (MIMS) was also applied, and its magnetic product was fed to a LIMS (700 G). This treatment was conducted for two particle size fractions of  $-106 + 74 \mu\text{m}$  and  $<74 \mu\text{m}$ .

### 3. Results and Discussions

#### 3.1. Sample Characterization

Table 1 presents the Fe content of the H<sub>2</sub>-reduced BR pellets measured through XRF, pXRF, ICP-MS, and QXRD methods. As known, the most reliable approach is XRF for this type of sample, which resulted in  $22 \pm 2$  wt% Fe. The amount of Fe measured through the portable XRF device was  $23 \pm 2$  wt%, while the QXRD and ICP-MS resulted in  $25 \pm 1$  wt% and  $25 \pm 1$  wt%, respectively. As can be seen in Table 1, for the feed sample, both XRF and pXRF results are in good correlation with each other, and the outcomes reported by Pilla et al. [9,24] are 22.7%. Aside from the feed, since the products of magnetic tests were analyzed through the pXRF method, the reliability of the data was essential for both non-magnetic and magnetic products. For this reason, through one case study, the correlation between the pXRF and XRF results is evaluated and given in Appendix A (Table A2). According to the results shown in Table A2 for three different samples, one can rely on the Fe contents measured through the pXRF device. It is important to note that the results presented in Table A2 were obtained for arbitrary three specimens containing Fe in the range of 22–36% to solely evaluate the reliability of the pXRF analyses and their correlations with the XRF results.

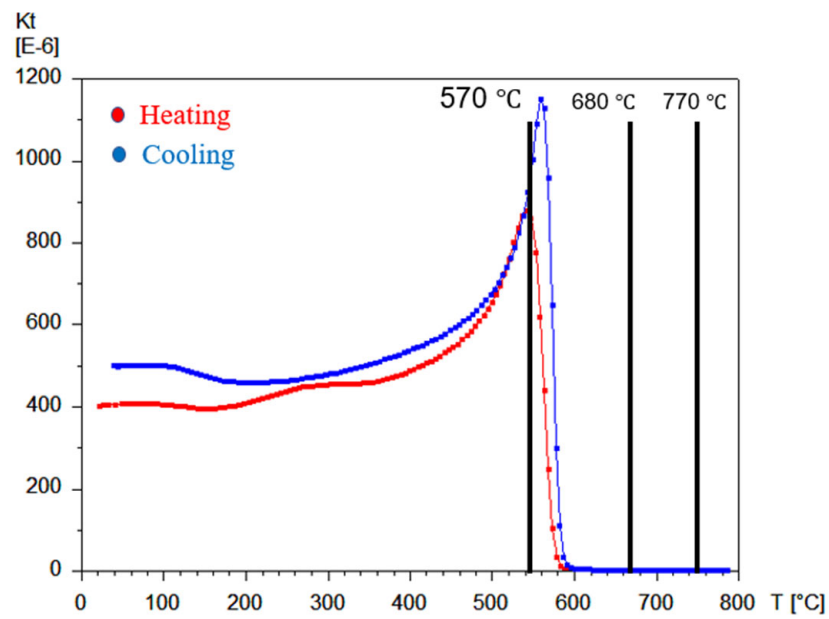
**Table 1.** Fe content measured through different analytical approaches on the feed sample.

Method	XRF	pXRF	ICP-MS	QXRD
Fe (wt%)	$22 \pm 2$	$23 \pm 2$	$25 \pm 1$	$25 \pm 1$

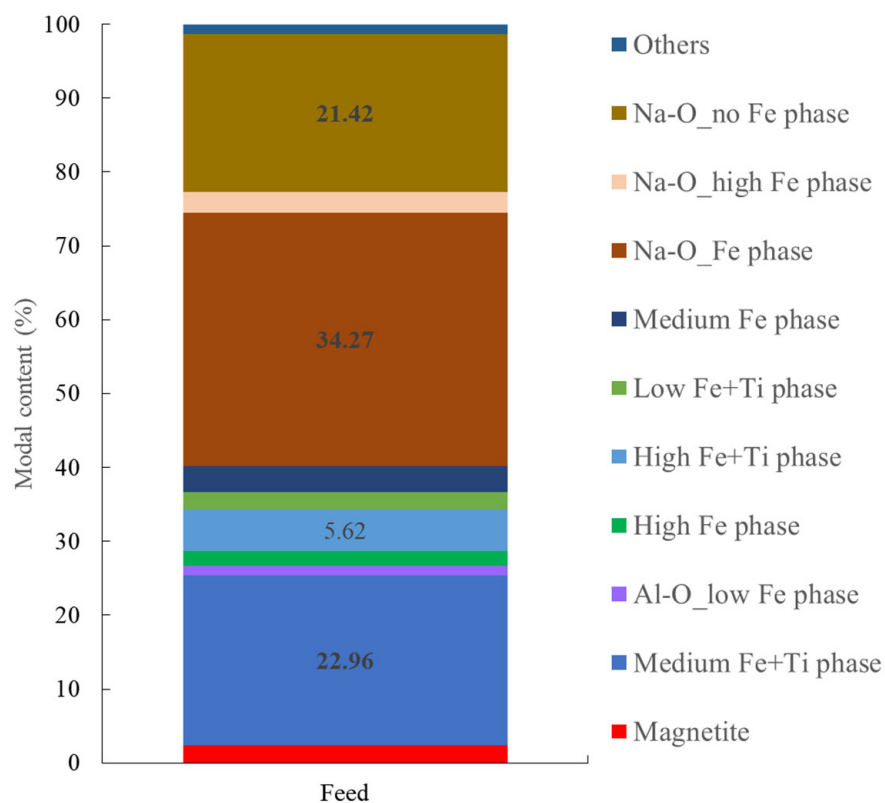
In addition, as the effect of particle size is evaluated through physical separation methods, the Fe content in different size fractions was measured through the pXRF analysis and reported in Appendix A (Figure A1). According to the results obtained, it can be concluded that there is no significant variation in the Fe amount at different particle ranges.

Figure 1 represents the thermomagnetic behavior of the sample at high temperatures (50–750 °C). The red and blue curves represent measurements during heating and cooling, respectively. As can be seen, there is a sudden peak at 570 °C, which represents the Curie temperature/point of magnetite [16]. Also, there are no peaks identified at 680 °C and 770 °C, which represent hematite and iron, respectively. Additionally, the Hopkinson effect can be observed from the curve, which is a feature of ferromagnetic materials in which an increase in the magnetic susceptibility is seen at temperatures between the blocking and the Curie temperatures of the material. The Hopkinson effect can be observed as a peak in thermomagnetic curves that immediately precedes the susceptibility drop associated with the Curie temperature [17]. In other words, Figure 1 demonstrates that the main iron-bearing component is magnetite, which is in line with the XRD results and automated mineralogy information presented below. Additionally, it shows the magnetic susceptibility of tested material, which will be discussed in detail in a separate futuristic work.

Figure 2 demonstrates the modal phases of the feed sample. Modal mineralogy data disclosed that only 2.35 wt% of the sample was composed of magnetite, and Fe is embedded in various phases. Regarding the level of iron in the Fe-containing phases in the sample, three groups were introduced: (i) a high Fe phase (40–60 wt%), (ii) a medium Fe phase (20–40 wt%), and (iii) a low Fe phase (Fe < 20 wt%). Other main phases were recognized as the Fe associated with Ti, Al, and Na, with different intensities. Around 21 wt% of the sample was Na-oxide rich, consisting of no Fe; 34 wt% of the sample contained Na associated with Fe; and 22 wt% and 5 wt% of the sample included medium and high Fe associated with Ti, respectively. According to the automated mineralogy results, the heterogeneous distribution of low/medium/high magnitudes of iron with other phases can potentially cause changes in separation processes. A detailed description of the liberation degree of the phases and their associations is given elsewhere [18].



**Figure 1.** Thermal magnetic susceptibility of studied H<sub>2</sub>-reduced bauxite residue using the Kappabridge method.



**Figure 2.** Modal phases of the post-processed ground pellets of H<sub>2</sub>-reduced bauxite residue before feeding to the magnetic separators.

Figure 3 shows the XRD phase pattern of raw BR and H<sub>2</sub>-reduced BR with 20 wt% NaOH at 500 °C for 2 h under 5 vol.% H<sub>2</sub> + 95 vol.% N<sub>2</sub>. Under these optimum conditions (BR with 20 wt% NaOH at 500 °C for 2 h under 5 vol.% H<sub>2</sub> + 95 vol.% N<sub>2</sub>), the conversion of hematite to magnetite reached a maximum of 96%. The detailed study of different parameters to find out the optimum reduction conditions was already discussed in the

study by Pilla et al. [9,19–24]. Reduction under the above-mentioned conditions shows that the phases of hematite ( $\text{Fe}_2\text{O}_3$ ) and goethite ( $\text{FeO}(\text{OH})$ ) were transformed into magnetite ( $\text{Fe}_3\text{O}_4$ ) according to Equation (2) under  $\text{H}_2$ .

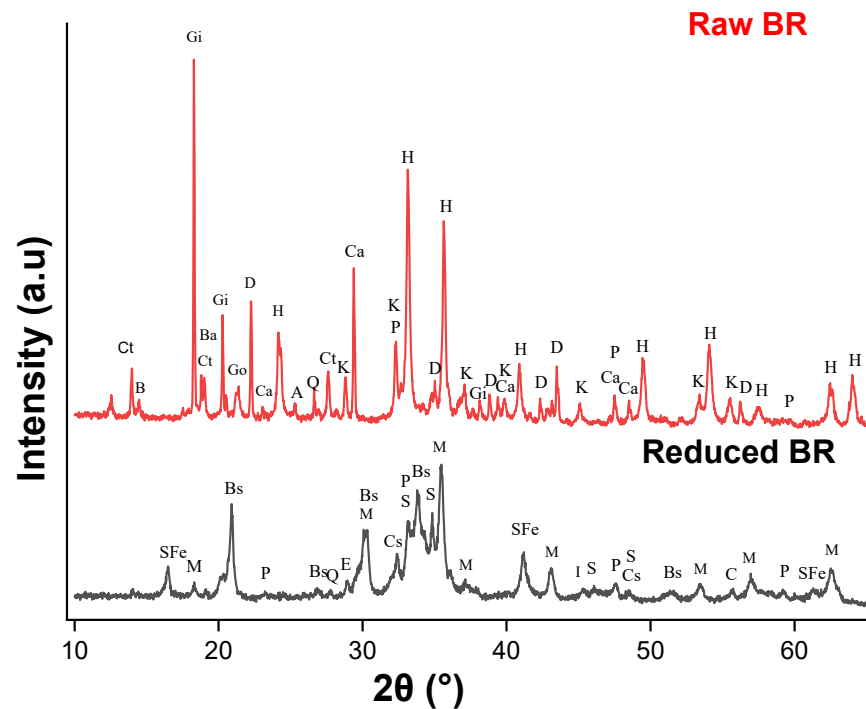
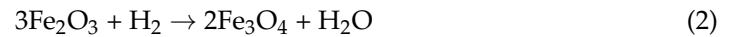


**Figure 3.** XRD analysis of raw and the  $\text{H}_2$ -reduced BR (at  $500\text{ }^\circ\text{C}$  for 2 h with 20 wt% NaOH, 5 vol.% (H—Hematite; D—Diaspore; Gi—Gibbsite; Go—Goethite; Ca—Calcite; Q—Quartz; B—Boehmite; Ba—Bayerite; Ct—Cancrinite; P—Perovskite; M—Magnetite; C—Calcium Iron Silicate; I—Iron; E—Sodium Calcium Silicate; Bs—Sodium Aluminum Silicate; SFe—Sodium Iron Oxide; S—Sodium Aluminate; K—Katoite; Cs—calcium silicate).

In addition to magnetite, the majority of the aluminum and silica reacted with NaOH (by decomposing into  $\text{NaO} > 300\text{ }^\circ\text{C}$ ) to produce water-leachable sodium aluminate, sodium aluminosilicate, and sodium-calcium silicate. The phases of titanium have existed as stable perovskites. The existence of water-leachable sodium iron ( $\text{NaFeO}_2$ ) oxide still existed, which can precipitate instantly as hematite during the water-leaching and magnetic separation downstream processes by dissolving excess  $\text{Na}^+$  in the water [9]. However, the  $\text{NaFeO}_2$  phase quantity is limited to 6.6 wt% according to QXRD results shown in Tables A3–A5 and does not significantly affect Fe recovery.

As depicted in Figure 4, fully reduced hematite to magnetite phases and sodium aluminate phases were visible in the SEM microstructure of the  $\text{H}_2$ -reduced BR sample ( $500\text{ }^\circ\text{C}$  for 120 min with 5 vol.%  $\text{H}_2$  + 95 vol.%  $\text{N}_2$ ). In addition, EDS showed the enriched magnetite Fe-fraction in the reduced BR matrix. These samples were further selected and processed for the extraction of iron through a sequential magnetic separation.

### 3.2. Magnetic Separation

#### 3.2.1. The Impact of Magnetic Intensity and Particle Size (Davis Tube and Slon<sup>®</sup> Tests)

Before conducting wet magnetic separation tests, several experiments at different size ranges were examined using a dry magnetic separator. A poor separation was recognized in a dry environment even for particles finer than  $<75\text{ }\mu\text{m}$  leading us to apply wet magnetic conditions. According to the principles of mineral processing as a function of particle size, effective magnetic separations are expected for particle sizes between  $75\text{--}1000\text{ }\mu\text{m}$



depending on the liberation degree of target minerals [25]. Figure 5 presents the iron content and its recovery at three different feed size fractions ( $-200 + 100 \mu\text{m}$ ,  $-100 + 75 \mu\text{m}$ , and  $<75 \mu\text{m}$ ) in the presence of two magnetic gradients, i.e., 1000 G and 2500 G. One can evidently observe that the iron grade for both magnetic intensities increases from 22% to 32%–34% for particle sizes of  $-200 + 100 \mu\text{m}$  and later reaches the maximum (40%) by reducing the size fraction to  $-100 + 75 \mu\text{m}$ . However, a further decrease in the particle range to  $<75 \mu\text{m}$  slightly reduces the Fe grade. According to the results shown in Figure 5, with respect to the variation of iron recovery versus particle size, the tendency depends on the applied magnetic field. At a lower magnetic field, i.e., 1000 G, recovery diminishes linearly from 80% to 55% by reducing the particle size from  $-200 + 100 \mu\text{m}$  to  $<75 \mu\text{m}$ . One plausible reason for such a trend is that coarser particles naturally have a higher mass and can be relatively easily captured and transported to the magnetic fraction (concentration) than the finer ones. Whereas, at a higher gradient of 2500 G, maximum recovery of 96% is acquired at the medium size fraction ( $-100 + 75 \mu\text{m}$ ), and reducing the particle size to  $<75 \mu\text{m}$  decreases the iron recovery to 72%. Therefore, by considering the maximization of both recovery and Fe content, the optimum particle size of  $-100 + 75 \mu\text{m}$  can be selected using 2500 G with one and/or two stages of scavenging/cleaning to recover the rest of the magnetic parts in the concentrate (i.e., magnetic products). It is also worth mentioning that part of the sample was soluble in the water and lost during all the experiments, which indeed persuades one to perform a few stages of water leaching (as a pre-retreatment step) before conducting the magnetic separation experiments for Na and Al recovery purposes. This phase was identified as a fully liberated Na-bearing phase, which composed approximately 21 wt% of the sample and was not associated with iron or other components (Figure 2).

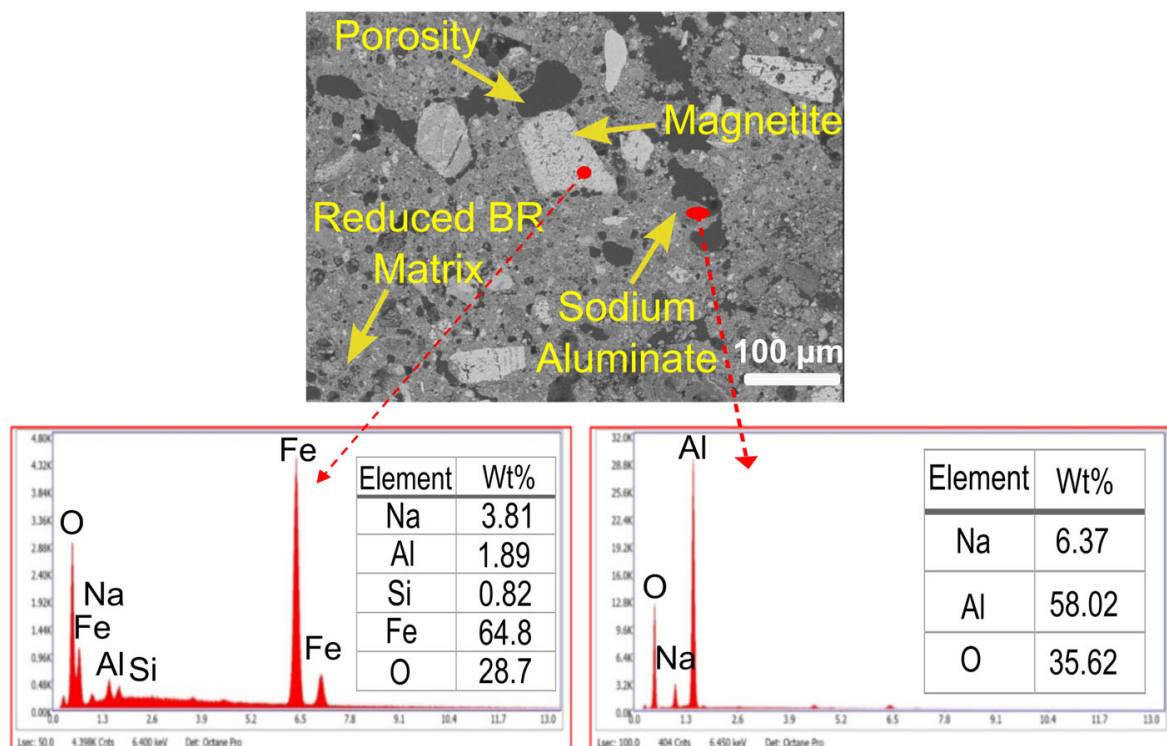
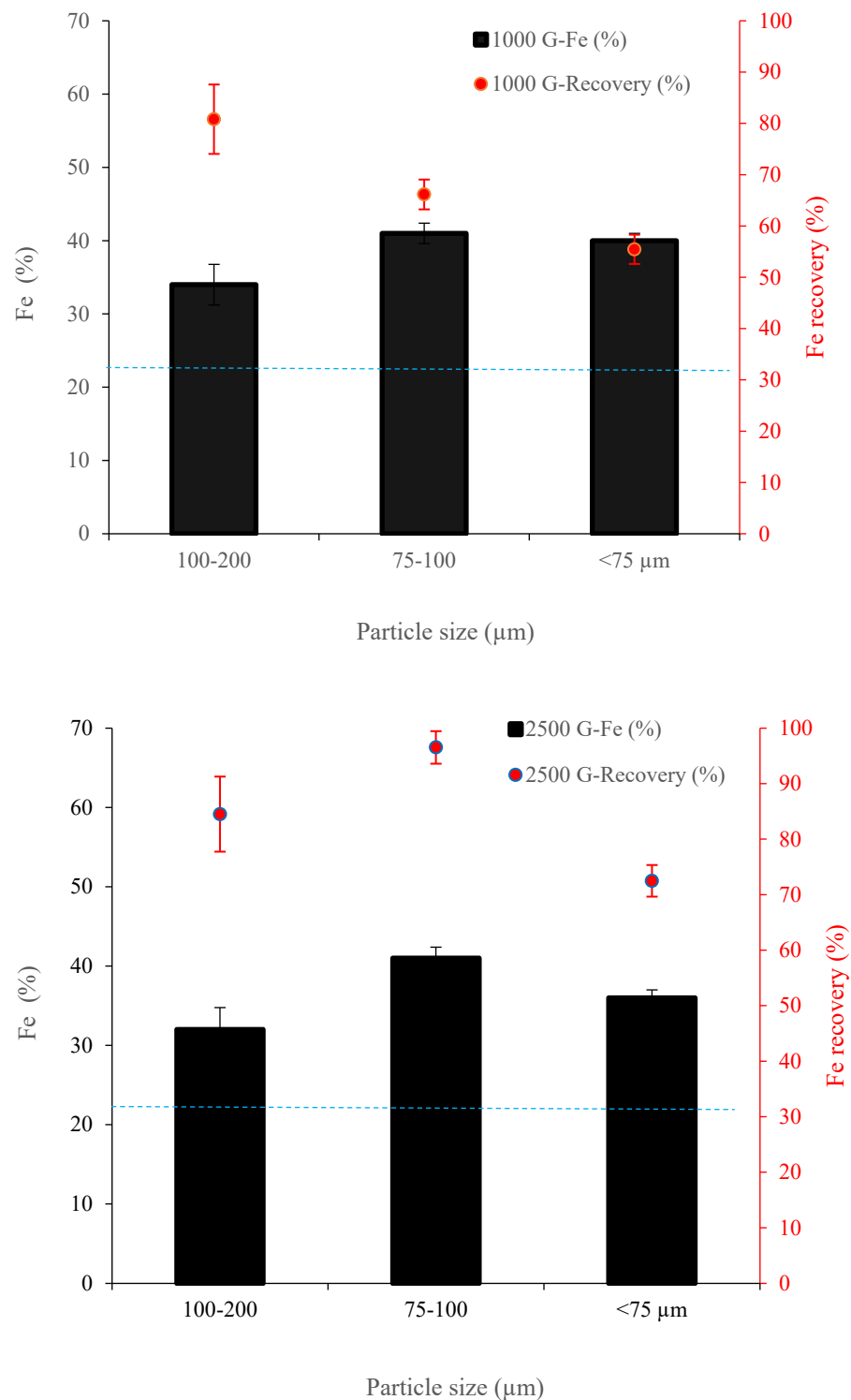


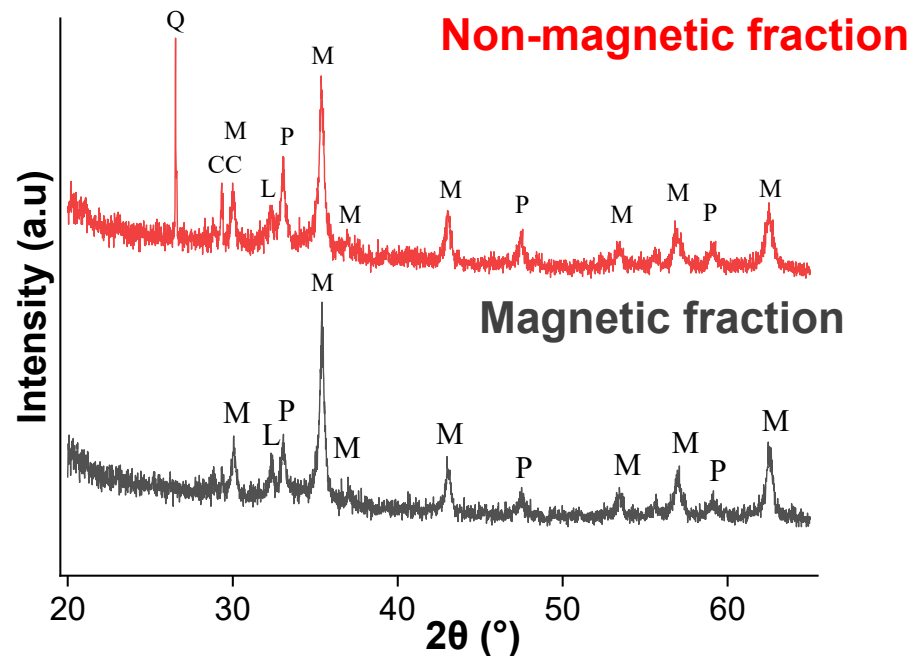
Figure 4. SEM-EDS analysis on the  $\text{H}_2$ -reduced BR.



**Figure 5.** The impact of particle size and magnetic field on separation efficiency using the Davis Tube (dash line represents the feed Fe content).

Figure 6 illustrates the XRD patterns of the magnetic and non-magnetic products from the separation tests in the Davis Tube. As shown in the magnetic product, magnetite is the main mineral phase; however, the peak intensities of perovskite and ilmenite were observed in minor fractions. Conversely, quartz, calcite, and perovskite phases were primarily enriched in the non-magnetic product, but the magnetite phase was still present with lower intensities. The comparable phase quantities of magnetic and non-magnetic products were measured through XRD Rietveld analysis (QXRD) and are displayed in

Table A5. Further, the phases of water-leachable sodium aluminates disappeared in both magnetic and non-magnetic fractions, which indicates that these phases were dissolved in the leach liquor. In other words, one pre-treatment stage, such as water leaching, can potentially remove these semi-soluble entities in order to relatively ease the downstream separation processes.



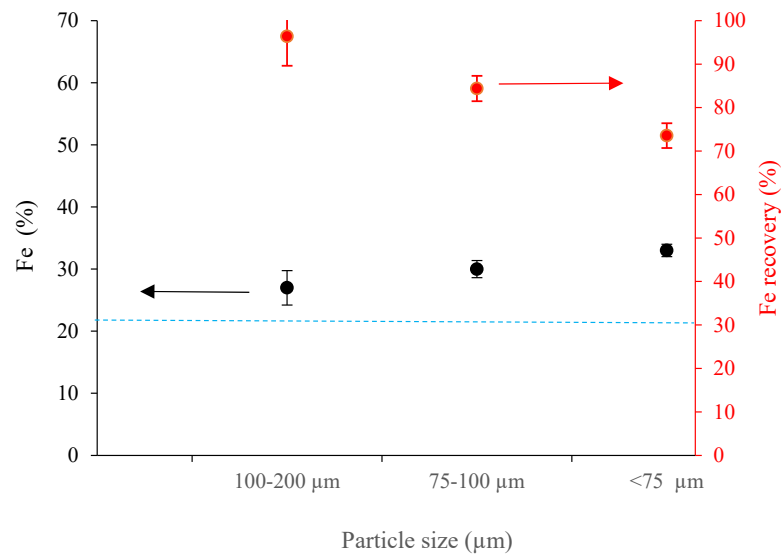
**Figure 6.** XRD patterns of non-magnetic and magnetic products of Davis Tube test (1000 G) (CC—Calcium Carbonate; Q—Quartz; P—Perovskite; M—Magnetite; L—Ilmenite).

Figure 7 illustrates the role of particle size in iron grade and its recovery obtained through Slon<sup>®</sup> experiments under a constant magnetic gradient of 1000 G. As can be seen, reducing particle size from  $-200 + 100 \mu\text{m}$  to  $<75 \mu\text{m}$  leads to an increase in iron grade from 27% to 33%, whereas the iron recovery diminishes from 96% to 73%. Enhancing Fe grade is most likely attributed to the increase in the liberation degree of iron-bearing phases, while the reduction in Fe recovery is caused by the attenuation of particle size. In this regard, Shao et al. [26] reported a similar trend of reducing hematite recovery by decreasing particle size. Most recently, Hassanzadeh et al. [27] investigated the effect of magnetic field and particle size on an  $\text{H}_2$ -reduced calcium-added bauxite residue. They found that coarsening the particle size from  $-106 + 74 \mu\text{m}$  to  $-212 + 106 \mu\text{m}$  at a constant magnetic gradient of 0.1 T diminished the Fe grade from 35% to 25% with an increase in iron recovery from 40% to 83%. Following this, Guo et al. [28] addressed the significant effect of particle size on magnetic separation processes and the requirement for their optimization for primary iron ore.

### 3.2.2. Wet Low-Intensity Magnetic Separation (WLIMS)

A common range of high solid content (10–17%  $w/w$ ) [29,30] together with a relatively lower level (3%  $w/w$ ) was chosen to investigate the impact of solid concentration on the separation efficiency of the studied sample. This lower level of solid content was considered to evaluate its impact on the selectivity of separation. Figure 8 exhibits the results of WLIMS with two different solid contents of 3% and 10% ( $w/w$ ) when the magnetic intensity and particle size were fixed at 350 G and  $-200 + 100 \mu\text{m}$ , respectively. It can be observed that increased solid content induced a recovery of 52% with a Fe grade of 33%. However, reducing the solid content resulted in higher selectivity, reaching a Fe grade of 40% and a relatively low recovery of 27%. One reason for such a phenomenon is related

to the transportation mechanism of the magnetic particles to the concentrates, which is more favorable at higher solid content (10% *w/w*). In this regard, Rayner and Napier-Munn [30] stated that capturing magnetic particles through a WLIMS test occurs through a flocculation process that proceeds rapidly at high pulp densities. By comparing the results of WLIMS (Figure 8) with the given outcomes from Davis Tube tests (Figure 5), which can be considered a medium-intensity magnetic separator (MIMS), one can conclude that either low or medium intensities cannot increase the Fe grade over 41%, but an acceptable degree of recovery can be obtained by these gradients. It is worth mentioning that the outcomes presented in Figure 8 are based on the data obtained through the experiments conducted without repetition. For this reason, further experimental tests should be undertaken for the sake of achieving a reasonable level of reproducibility for the obtained results.



**Figure 7.** The impact of particle size on iron grade and its recovery in Slon<sup>®</sup> magnetic tests (dash line represents the initial iron feed grade).

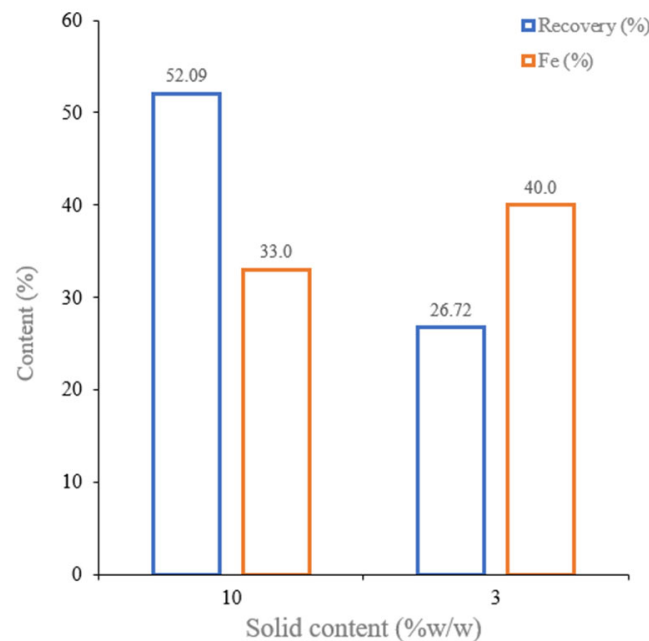


**Figure 8.** The effect of solid content on the WLIMS tests.

According to the results presented in Figure 8, a two-stage magnetic separation process was applied using the flowsheet given in Figure 9, i.e., a medium-intensity magnetic separator (3000 G) followed by a low-intensity one (700 G). Both pieces of equipment were operated in a wet medium at similar technical conditions. The results of these experiments are presented in Table 2 per stream. As seen, the final iron contents of magnetic products for size fractions of  $-100 + 75 \mu\text{m}$  and  $<75 \mu\text{m}$  through the two-stage treatment were 32% and 36%, respectively. Applying only one stage of MIMS led to about 95% recovery, while the Fe content was not beneficiated significantly due to the transportation of most of the magnetite-bearing phases to the concentrate as well as a relatively high magnetic field, i.e., 3000 G. By applying one more stage (i.e., LIMS) on the magnetic product of the MIMS unit, the Fe content increased from an initial value of ca. 22% to 32% for coarse particle fraction. The total recovery can be calculated through Equation (3), which resulted in 94% for the  $-100 + 75 \mu\text{m}$  particle size.

$$R_{total}(\%) = \frac{R_{MIMS}}{100} \times \frac{R_{LIMS}}{100} \times 100 \tag{3}$$

where the  $R_{MIMS}$  and  $R_{LIMS}$  are the recoveries of medium-intensity and low-intensity magnetic separations, respectively.

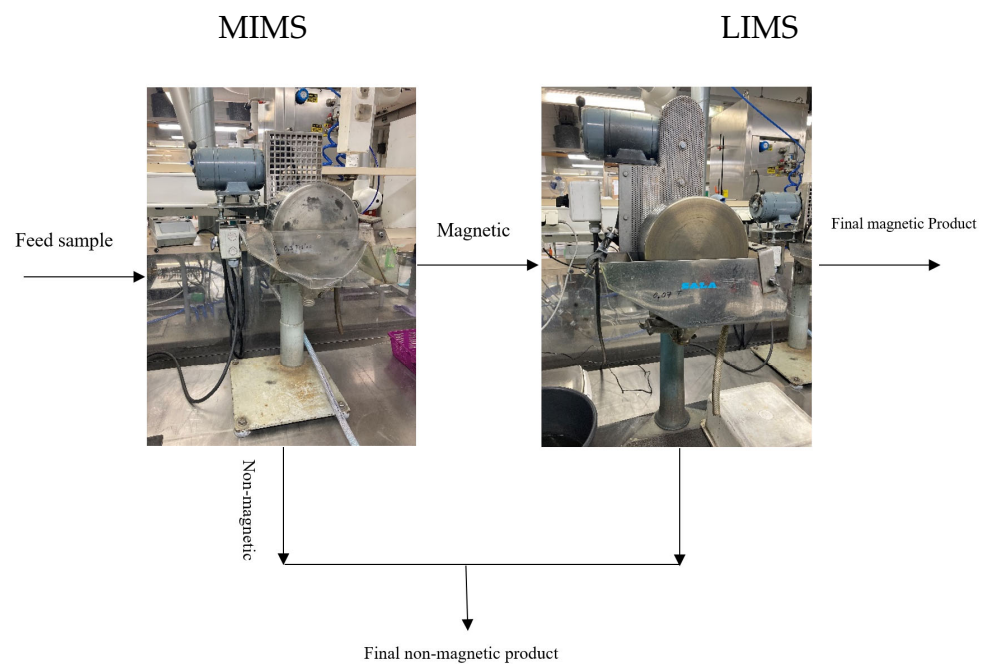


**Figure 9.** A schematic flowsheet of sample treatment using a medium followed by low-intensity magnetic separators.

**Table 2.** The results of a two-stage magnetic separation (MIMS followed by LIMS).

Stream	$-100 + 75 \mu\text{m}$		$-75 \mu\text{m}$	
	Mass (g)	Fe (%)	Mass (g)	Fe (%)
MIMS Mag	98.98	23 *	117.25	24 *
MIMS Non-Mag	8.88	13	51.17	19
LIMS Mag	70.11	32	68.83	36
LIMS Non-Mag	23.89	26	43.88	29

\* Obtained values via mass balancing of the circuit.

#### 4. Conclusions and Future Works

The present study aimed at investigating the reduction of BR with hydrogen, with a special focus on iron extraction through magnetic separation processes. To produce an intermediate material rich in magnetite and sodium aluminate, BR was combined with NaOH and then reduced with hydrogen. This enabled the recovery of iron, aluminum, and sodium as a succeeding step. Following reduction roasting in the presence of 5 vol.% H<sub>2</sub> gas at 500 °C for 2 h with 20 wt% NaOH, iron oxides and ferric oxyhydroxide (Fe<sub>2</sub>O<sub>3</sub>, FeOOH), and aluminum (oxy)hydroxide oxides (Al(OOH), Al(OH)<sub>3</sub>) were converted into magnetite (Fe<sub>3</sub>O<sub>4</sub>) and sodium aluminates (NaAlO<sub>2</sub>). This conversion was verified using the XRD, automated mineralogy, and thermomagnetic analysis results. The AM results showed that the complexity of the feed sample, the association of Fe-bearing entities with other phases, and the fine dissemination of the iron throughout the matrix could potentially lead to serious challenges in recovering Fe through the conventional magnetic separation processes. It was found that increasing magnetic intensity from 1000 G to 2500 G resulted in increased recovery for all studied size fractions in the Davis Tube tests. It was concluded that a particle range of  $-100 + 75 \mu\text{m}$  can be the most appropriate size to achieve the maximum Fe content of 41% with various recoveries depending on the magnetic field and type of equipment. Results of WLIMS (350 G) confirmed the given maximum Fe grade but revealed less recovery even at 10% (*w/w*) solid concentration compared to the Davis Tube. Overall, the H<sub>2</sub> reduction-magnetic separation process found a promising metal recovery technology in terms of sustainability and zero waste valorization of BR. Further research is needed to enhance the Fe recovery and grade along with other value-added metals (e.g., REEs and Ti) recovery in this route.

According to the results presented in this work and the recent research studies found in the literature, the following highlights have been considered for future works:

- Further experimental studies to acquire an in-depth understanding of the sample characterization using micro-computed tomography with respect to the significant difference in X-ray adsorption densities between Ti- and Fe-bearing phases and Na, Ca-embedded phases;
- Applying intensive grinding/ultrafine grinding to reach a reasonable liberation degree of magnetite at particle sizes below 20–10  $\mu\text{m}$ ;
- Using physicochemical-based approaches such as flocculation, flotation, and flocculation-flotation on ultrafine ground particles;
- Increasing the reduction temperature to above 900 °C in order to coarsen the Fe particles and potentially ease the downstream separation processes.

**Author Contributions:** Conceptualization, A.H.; methodology, A.H. and G.P.; software, A.H. and M.K.K.; validation, A.H. and P.B.K.; formal analysis, A.H. and G.P.; investigation, A.H. and G.P.; resources, A.H.; data curation, A.H., G.P. and M.K.K.; writing—original draft preparation, A.H.; writing—review and editing, A.H., G.P., M.K.K. and P.B.K.; visualization, A.H.; supervision, A.H. and P.B.K.; project administration, A.H. and P.B.K.; funding acquisition, P.B.K. All authors have read and agreed to the published version of the manuscript.

**Funding:** This study was performed and financially supported by The European Union's Horizon 2020 research and innovation program under grant number 958307 (HARARE project).

**Data Availability Statement:** Data will be provided per request.

**Acknowledgments:** Authors would like to thank Nathan Church, Marius Schjølberg, Kornel Mateusz Tobiczkyk, Camilo Mena Silva, Stefanie Lode, Gustav Ward, Laurentius Tjihuis, Jesper Hansen Levinssen, and Henning Leonard Nygård Aune, from the Norwegian University of Science and Technology and Yiannis Pontikes and Tobias Hertel from Katholieke Universiteit Leuven for their assistance. We acknowledge the Research Council of Norway for supporting the Norwegian Laboratory for Mineral and Materials Characterisation, MiMaC with project number of 269842/F50.

**Conflicts of Interest:** There is no conflict of interest.

## Appendix A

Tap water characteristic was measured through the ICP-MS method during the measurements at the NTNU Mineral Processing laboratory.

**Table A1.** Properties of tap water used for the measurements.

Component	Mg	S	Ca	Mn	Fe	Co	Ni	Cu	Zn	Sr
Concentration * (ng/mL)	913.49	649.37	21566.67	0.15	110.67	0.07	1.29	14.72	1.32	52.97

\* The values are the average of three measurements. The amounts of other trace elements were as Ag < 0.03, Cd < 0.06, Pb < 0.002, and U < 0.05.

Table A2 represents a comparison between pXRF and XRF results for three various samples used in this work.

**Table A2.** XRF versus pXRF for three different samples.

Sample Type	Sample 01		Sample 02		Sample 03: Feed Sample	
Element	pXRF * (wt%)	XRF (wt%)	pXRF * (wt%)	XRF (wt%)	pXRF * (wt%)	XRF (wt%)
Th	0.013	0.012	0.009	0.010	0.01	0.015
Zr	0.076	<0.050	0.079	<0.050	0.079	0.075
Pb	0.011	0.014	0.011	0.032	0.020	0.01
Zn	0.0077	0.007	0.007	0.005	0.004	0.002
Cu	0.005	0.009	0.055	0.007	<LOD	0.008
Ni	0.077	0.077	0.059	0.070	0.060	0.05
<b>Fe</b>	<b>35.90</b>	<b>36.50</b>	<b>25.65</b>	<b>26.84</b>	<b>23.40</b>	<b>22.7</b>
Cr	0.22	0.160	0.179	0.147	0.156	0.18
Ti	3.27	3.240	3.040	3.007	2.77	3.05
Ca	6.47	7.190	6.313	6.953	5.46	5.93
Al	6.8	7.319	7.900	9.052	7.31	12.48
Si	3.185	4.730	2.970	4.140	2.40	3.51
Mg	1.44	0.3	0.025	0.118	<LOD **	0.12

\* The values are the average of measurements from three different points. \*\* LOD stands for values lower than the detection limit of the equipment.

Tables A3–A5 indicates the phases measured through XRD Rietveld of raw BR, H<sub>2</sub>-reduced BR, and magnetic and non-magnetic fraction, respectively.

**Table A3.** Mineralogy of the raw BR (dried) analyzed by the XRD Rietveld quantification (QXRD).

Phase	Formula	Raw BR (wt%)
Hematite	Fe <sub>2</sub> O <sub>3</sub>	32.6
Goethite	FeOOH	5.2
Cancrinite	Na <sub>6</sub> Ca <sub>2</sub> [(CO <sub>3</sub> ) <sub>2</sub>   Al <sub>6</sub> Si <sub>6</sub> O <sub>24</sub> ]·2H <sub>2</sub> O	12.8
Gibbsite	γ-Al(OH) <sub>3</sub>	3.4
Perovskite	CaTiO <sub>3</sub>	2.2
Katoite	Ca <sub>3</sub> Al <sub>2</sub> (SiO <sub>4</sub> ) <sub>3</sub>	12.7
Diaspore	α-AlOOH	15.2
Calcite	CaCO <sub>3</sub>	6.0
Quartz	SiO <sub>2</sub>	0.3

**Table A3.** *Cont.*

Phase	Formula	Raw BR (wt%)
Boehmite	$\gamma\text{-AlOOH}$	2.7
Anatase	$\text{TiO}_2$	0.9
Bayerite	$\alpha\text{-Al(OH)}_3$	1.4
Amorphous/not detected	-	4.5

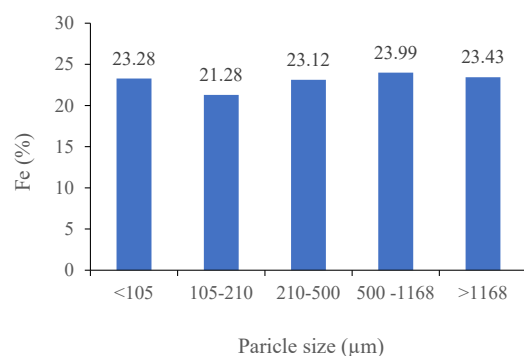
**Table A4.** Mineralogy of the  $\text{H}_2$ -reduced BR analyzed by XRD Rietveld quantification (QXR).

Phase	Formula	$\text{H}_2$ -Reduced BR (wt%)
Magnetic	$\text{Fe}_3\text{O}_4$	35.5
Quartz	$\text{SiO}_2$	0.2
Perovskite	$\text{CaTiO}_3$	5.9
Sodium aluminum silicate	$\text{Na}_{12}\text{AlSiO}_5$	11.9
Sodium aluminate	$\text{NaAlO}_2$	29.5
Iron	$\text{Fe}$	0.7
Sodium iron oxide	$\text{NaFeO}_2$	6.6
Calcium iron silicate	$\text{Ca(Fe)SiO}_3$	0.5
Sodium calcium silicate	$(\text{Na})\text{CaSiO}_3$	0.9
Calcium silicate	$\text{CaSiO}_3$	1.5
Amorphous/not detected	-	6.6

**Table A5.** Mineralogy of the magnetic and non-magnetic products analyzed by XRD Rietveld quantification (QXR).

Phase	Formula	Magnetic Product (wt%)	Non-Magnetic Product (wt%)
Magnetite	$\text{Fe}_3\text{O}_4$	61.6	37.8
Perovskite	$\text{CaTiO}_3$	12.4	18.9
Ilmenite	$\text{FeTiO}_3$	3.9	4.1
Quartz	$\text{SiO}_2$	-	7.5
Calcite	$\text{CaCO}_3$	-	5.9
Amorphous/not detected	-	22.1	25.8

Figure A1 displays the Fe amount in different size fractions indicating that the sieving process does not improve the Fe content.

**Figure A1.** Fe content in different size fractions.



## References

1. Dyussenova, S.; Abdulvaliyev, R.; Akcil, A.; Gladyshev, S.; Ruzakhunova, G. Processing of low-quality gibbsite-kaolinite bauxites. *Metals* **2022**, *12*, 1030. [CrossRef]
2. Swain, B.; Akcil, A.; Lee, J. Red mud valorization an industrial waste circular economy challenge; review over processes and their chemistry. *Crit. Rev. Environ. Sci. Technol.* **2022**, *52*, 520–570. [CrossRef]
3. Borra, C.R.; Blanpain, B.; Pontikes, Y.; Binnemans, K.; Van Gerven, T. Recovery of rare earths and other valuable metals from bauxite residue (red mud): A review. *J. Sustain. Metall.* **2016**, *2*, 365–386. [CrossRef]
4. Evans, K. The History, Challenges, and New Developments in the Management and Use of Bauxite Residue. *J. Sustain. Metall.* **2016**, *2*, 316–331. [CrossRef]
5. Xue, S.; Zhu, F.; Kong, X.; Wu, C.; Huang, L.; Huang, N.; Hartley, W. A review of the characterization and revegetation of bauxite residues (Red mud). *Environ. Sci. Pollut. Res. Int.* **2016**, *23*, 1120–1132. [CrossRef]
6. Sutar, H.; Mishra, S.C.; Sahoo, S.K.; Chakraverty, A.P.; Maharana, H.S. Progress of red mud utilization: An overview. *Am. Chem. Sci. J.* **2014**, *4*, 255–279. [CrossRef]
7. Zeng, H.; Lyu, F.; Sun, W.; Zhang, H.; Wang, L.; Wang, Y. Progress on the industrial applications of red mud with a focus on China. *Minerals* **2020**, *10*, 773. [CrossRef]
8. Hertel, T.; Pontikes, Y. Geopolymers, inorganic polymers, alkali-activated materials and hybrid binders from bauxite residue (red mud)—Putting things in perspective. *J. Clean. Prod.* **2020**, *258*, 120610. [CrossRef]
9. Pilla, G.; Kapelari, S.V.; Hertel, T.; Blanpain, B.; Pontikes, Y. Hydrogen reduction of bauxite residue and selective metal recovery. *Mater. Today Proc.* **2022**, *57*, 705–710. [CrossRef]
10. Kapelari, S.; Gamaletsos, P.N.; Donck, T.V.D.; Pontikes, Y.; Blanpain, B. H<sub>2</sub>-based processes for Fe and Al recovery from bauxite residue (red mud): Comparing the options. *Mater. Proc.* **2021**, *5*, 45. [CrossRef]
11. Li, Y.; Wang, J.; Wang, X.; Wang, B.; Luan, Z. Feasibility study of iron mineral separation from red mud by high gradient superconducting magnetic separation. *Phys. C Supercond.* **2011**, *471*, 91–96. [CrossRef]
12. Rai, S.; Nimje, M.T.; Chaddha, M.J.; Modak, S.; Rao, K.R.; Agnihotri, A. Recovery of iron from bauxite residue using advanced separation techniques. *Miner. Eng.* **2019**, *134*, 222–231. [CrossRef]
13. Cardenia, C.; Balomenos, F.; Panias, D. Iron recovery from bauxite residue through reductive roasting and Wet Magnetic Separation. *J. Sustain. Metall.* **2019**, *5*, 9–19. [CrossRef]
14. Hassanzadeh, A.; Pilla, G.; Hertel, T.; Pontikes, Y.; Kowalczyk, P.B. H<sub>2</sub>-reduction of bauxite residue and iron recovery through magnetic separation. In Proceedings of the 17th International Mineral Processing Symposium (IMPS), Istanbul, Turkey, 15–17 December 2022; pp. 223–243.
15. McEnroe, S.A.; Church, N.; Fabian, K.; Stange, M.F.; Helvoort, A.T.J. An enigma in rock magnetism: Can microstructures in magnetite cause a threefold increase in the efficiency of NRM acquisition in the Stardalur Basalts? *Geophys. J. Int.* **2022**, *231*, 835–855. [CrossRef]
16. Fabian, K.; Shcherbakov, V.P.; McEnroe, S.A. Measuring the Curie temperature. *Geochem. Geophys. Geosyst.* **2013**, *14*, 947–961. [CrossRef]
17. Franco, V.; Dodrill, B. *Magnetic Measurement Techniques for Materials Characterization*; Springer: New York, NY, USA, 2021; ISBN 978-3-030-70443-8. [CrossRef]
18. Hassanzadeh, A.; Lode, S.; Pilla, G.; Røstad, J.; Kowalczyk, P.B. Complementary approaches in characterization of secondary raw materials: A case study of H<sub>2</sub>-reduced bauxite residue. In Proceedings of the Process Mineralogy'22, MEI Conferences, Sitges, Spain, 2–4 November 2022.
19. Pilla, G.; Hertel, T.; Kapelari, S.; Blanpain, B.; Pontikes, Y. Reactions and Phase Transformations During the Low-Temperature Reduction of Bauxite Residue by H<sub>2</sub> in the Presence of NaOH, and Recovery Rates Downstream. In Proceedings of the 40th International ICSOBA Conference, Athens, Greece, 10–14 October 2022; TRAVAUX 51. pp. 801–810.
20. Kapelari, S.; Gamaletsos, P.N.; Pilla, G.; Pontikes, Y.; Blanpain, B. Developing a Low-Temperature, Carbon-Lean Hybrid Valorisation Process for Bauxite Residue (Red Mud) Towards Metallic Fe and Al Recovery. *J. Sustain. Metall.* **2023**, 1–10. [CrossRef]
21. Coelho, A.A. TOPAS-Academic; A Computer Programme for Rietveld Analysis. Available online: <http://www.topas-academic.net/> (accessed on 20 April 2023).
22. Jansen, D.; Goetz-Neunhoeffer, F.; Stabler, C.; Neubauer, J. A remastered external standard method applied to the quantification of early OPC hydration. *Cem. Concr. Res.* **2011**, *41*, 602–608. [CrossRef]
23. Fernandes, I.B.; Rudolph, M.; Hassanzadeh, A.; Bachmann, K.; Meskers, C.; Peuker, U.; Reuter, M.A. The quantification of entropy for multicomponent systems: Application to microwave-assisted comminution. *Miner. Eng.* **2021**, *170*, 107016. [CrossRef]
24. Pilla, G.; Hertel, T.; Blanpain, B.; Pontikes, Y. Influence of H<sub>2</sub> content on Fe, Al and Na recovery during low-temperature reduction of bauxite residue. In Proceedings of the 8th International Slag Valorisation Symposium, Mechelen, Belgium, 18–20 April 2023; pp. 146–149.
25. Drzymala, J. *Mineral Processing Foundations of Theory and Practice of Minerallurgy*, 1st ed.; Wroclaw University of Technology: Wroclaw, Poland, 2007; pp. 1–497. ISBN 978-83-7493-362-9.
26. Shao, Y.; Veasey, T.J.; Rowson, N.A. Wet high intensity magnetic separation of iron minerals. *Magn. Electr. Sep.* **1996**, *8*, 41–51. [CrossRef]

27. Hassanzadeh, A.; Kar, M.K.; Safarian, J.; Kowalczyk, P.B. An Investigation on Reduction of Calcium Added Bauxite Residue Pellets by Hydrogen and Iron Recovery through Physical Separation Methods. *Metals* **2023**, *13*, 946. [[CrossRef](#)]
28. Guao, X.; Zhang, M.; Ren, W.; Dai, S. Influence of particle size on the magnetism of magnetite and the development of an energy-efficient three-product magnetic separator. *Sep. Sci. Technol.* **2021**, *56*, 1397–1406. [[CrossRef](#)]
29. Xiong, W.; Deng, J.; Chen, B.; Deng, S.; Wie, D. Flotation-magnetic separation for beneficiation of rare earth ores. *Miner. Eng.* **2018**, *119*, 49–56. [[CrossRef](#)]
30. Rayner, J.G.; Napier-Munn, T.J. The mechanism of magnetics capture in the wet drum magnetic separator. *Miner. Eng.* **2000**, *13*, 277–285. [[CrossRef](#)]

**Disclaimer/Publisher's Note:** The statements, opinions and data contained in all publications are solely those of the individual author(s) and contributor(s) and not of MDPI and/or the editor(s). MDPI and/or the editor(s) disclaim responsibility for any injury to people or property resulting from any ideas, methods, instructions or products referred to in the content.